RAA 2019 Vol. **19** No. **11**, 158(10pp) doi: 10.1088/1674–4527/19/11/158

http://www.raa-journal.org *http://iopscience.iop.org/raa*

Research in Astronomy and Astrophysics

The Lyman-alpha Solar Telescope (LST) for the ASO-S mission — I. Scientific objectives and overview

Hui Li[1,2], Bo Chen[3], Li Feng[1,2], Ying Li[1,2], Yu Huang[1,2], Jing-Wei Li[1,2], Lei Lu[1,2], Jian-Chao Xue[1,2], Bei-Li Ying[1,2], Jie Zhao[1,2], Yu-Tong Yang[1,2], Wei-Qun Gan[1,2], Cheng Fang[4], Ke-Fei Song[3], Hong Wang[5], Quan-Feng Guo[3], Ling-Ping He[3], Bo Zhu[5], Cheng Zhu[6], Lei Deng[6], Hai-Chao Bao[6], Cai-Xia Cao[6] and Zhong-Guang Yang[6]

[1] Key Laboratory of Dark Matter and Space Astronomy, Purple Mountain Observatory, Chinese Academy of Sciences, Nanjing 210034, China; *nj.lihui@pmo.ac.cn*
[2] School of Astronomy and Space Science, University of Science and Technology of China, Hefei 230026, China
[3] Changchun Institute of Optics, Fine Mechanics and Physics, Chinese Academy of Sciences, Changchun 130033, China
[4] School of Astronomy and Space Science, Nanjing University, Nanjing 210023, China
[5] Xi'an Institute of Optics and Precision Mechanics, Chinese Academy of Sciences, Xi'an 710119, China
[6] Innovation Academy for Microsatellites, Chinese Academy of Sciences, Shanghai 201210, China

Received 2019 June 28; accepted 2019 July 25

Abstract As one of the payloads for the Advanced Space-based Solar Observatory (ASO-S) mission, the Lyman-alpha (Lyα) Solar Telescope (LST) is aimed at imaging the Sun and the inner corona up to 2.5 $R_\odot$ (mean solar radius) in both the Lyα (121.6 nm) and visible wavebands with high temporo-spatial resolution, mainly targeting solar flares, coronal mass ejections (CMEs) and filaments/prominences. LST observations allow us to trace solar eruptive phenomena from the disk center to the inner corona, to study the relationships between eruptive prominences/filaments, solar flares and CMEs, to explore the dynamical processes and evolution of solar eruptions, to diagnose solar winds, and to derive physical parameters of the solar atmosphere. LST is actually an instrument suite, which consists of a Solar Disk Imager (SDI), a Solar Corona Imager (SCI), a White-light Solar Telescope (WST) and two Guide Telescopes (GTs). This is the first paper in a series of LST-related papers. In this paper, we introduce the scientific objectives, present an overview of the LST payload and describe the planned observations. The detailed design and data along with potential diagnostics are described in the second (Paper II) and third (Paper III) papers, respectively, appearing in this issue.

Key words: Sun: flares — Sun: coronal mass ejections (CMEs) — Sun: filaments, prominences — Sun: corona — Sun: chromosphere — Sun: UV radiation

1 INTRODUCTION

The solar atmosphere is always dynamical. As the two most energetic eruptions on the Sun and the primary drivers of disturbed (sometimes disastrous) space weather (Schwenn 2006), solar flares and coronal mass ejections (CMEs) are usually the targets of both ground-based and space-borne solar telescopes and instruments. Ground-based telescopes are capable of achieving high spatial resolution with large apertures and adaptive optics (AO) but they lack continuity of observation. Space-borne instruments have the advantage of continuous observation and open windows of observations in shorter wavelengths which are absorbed by the Earth's atmosphere.

In the past decades, quite a few solar missions have been flown in space and have provided both imaging and spectroscopic data with high quality. Studies conducted with these data have widened and deepened our knowledge and comprehensive understanding of the Sun and its activity. Full-disk imaging observations have been conducted by, e.g., the Extreme-ultraviolet Imaging Telescope (EIT) (Delaboudinière et al. 1995) onboard the very successful Solar and Heliospheric Observatory (SOHO) mission (Domingo et al. 1995) in four extreme ultraviolet (EUV) wavebands with relatively low

temporo-spatial resolution due to limited telemetry, and the Atmospheric Imaging Assembly (AIA) (Lemen et al. 2012) onboard the Solar Dynamics Observatory (SDO) mission (Pesnell et al. 2012) in seven EUV and two far ultraviolet (FUV) wavebands with high temporo-spatial resolution, thanks to its geostationary orbit. Imaging observations of the corona have been made, e.g., by the Large Angle Spectroscopic Coronagraph (LASCO) suite (Brueckner et al. 1995) onboard the SOHO mission with relatively low temporo-spatial resolution due again to the low telemetry available, but with capability of revealing faint structures and CMEs in the corona because of the low stray-light and wide dynamical range; and by the Sun Earth Connection Coronal and Heliospheric Investigation (SECCHI) package (Howard et al. 2008) onboard the Solar TErrestrial RElations Observatory (STEREO) mission (Kaiser et al. 2008) with relatively high temporal resolution. The Multi Element Telescope for Imaging and Spectroscopy (METIS) coronagraph on the Solar Orbiter mission will provide imaging observations in both the Lyα and visible wavebands with higher temporo-spatial resolution (Antonucci et al. 2019).

However, as is well known, we are still lacking simultaneous observations of the full disk and corona in the same waveband by a single payload or mission. The Lyman-alpha Solar Telescope (LST) payload (Li 2016) of the Advanced Space-based Solar Observatory (ASO-S) mission (Gan et al. 2019) will fill this gap. The basic idea of the LST payload for ASO-S mission comes from the Lyman-alpha Orbital Telescope (LYOT) for the proposed France-China joint mission – SMall Explorer for Solar Eruptions (SMESE) (Vial et al. 2007), but some modifications and expansions have been made to fulfill the scientific objectives of the ASO-S mission.

The LST payload is designed to image the full disk of the Sun and the inner corona up to 2.5 $R_\odot$ ($R_\odot$ stands for the mean solar radius) simultaneously for the first time in both the Lyα line and white-light (WL) with a suite of instruments, including a Solar Disk Imager (SDI), a Solar Corona Imager (SCI), a White-light Solar Telescope (WST) and two Guide Telescopes (GTs). The objectives are to trace solar eruptive phenomena from the disk center to the inner corona, to explore the relationships between eruptive prominences, solar flares and CMEs, to study the dynamical processes and evolution of solar eruptions, to diagnose solar winds, and to derive physical parameters of the solar atmosphere.

We choose the neutral hydrogen Lyα line for simultaneous observation of the full-disk and the inner corona because it is the brightest vacuum ultraviolet (VUV) line and is very powerful in diagnosing structures in the solar atmosphere with a wide temperature range (from the chromosphere to the corona) (e.g., Schühle et al. 2011). In the corona, it is predominantly formed by resonant scattering of the intense underlying chromospheric Lyα emission. The Lyα line is sensitive to the magnitude and orientation of the magnetic field and its intensity is related to the outflow velocity of the scattering species due to the Doppler dimming effect (e.g., Hyder & Lites 1970; Esser & Habbal 1993; Dolei et al. 2018). The full-disk irradiance in the Lyα line changes with solar cycle and at solar maximum its value is double that at solar minimum. The Transition Region and Coronal Explorer (TRACE) (Handy et al. 1999b) has taken some images of parts of the solar disk with contamination from other wavebands due to the incomplete suppression of emission from longer wavelengths (Handy et al. 1999a). Observations with subarcsecond resolution of the Sun in the Lyα line from the Very high Angular resolution ULtraviolet Telescope (VAULT) have elucidated the dynamical structures of the chromosphere and the low transition region, and demonstrated the applicability of this line for the study of these regions (Vourlidas et al. 2010, 2016). During solar flares, the irradiance of the Lyα line increases intensively as demonstrated by observations by the Geostationary Operational Environmental Satellites (GOES) EUV sensor (EUVS) band E (Lyα) and the Extreme Ultraviolet Variability Experiment (EVE) (Woods et al. 2012) onboard SDO (Fig. 1). Observations and simulations indicate that it is beneficial for flare diagnosis (e.g., Hong et al. 2019). Due to these characteristics, the Lyα line should open a completely new window to observe the Sun. Many proposed instruments, such as the Extreme Ultraviolet Imager (EUI) and METIS payload on the Solar Orbiter mission and Lyman Alpha Spicule Observatory (LASSO) will observe the Sun in this line. LST has the advantage of being able to continuously observe the Sun (Li 2016).

We organize this paper (Paper I) in the following structure. We describe the scientific objectives of the LST payload in Section 2, and present an overview of the LST payload in Section 3; we describe the planned LST observations in Section 4 and finally we summarize the paper in Section 5. Paper II (Chen et al. 2019) presents the detailed design of the payload, and Paper III (Feng et al. 2019) the data and potential diagnostics.

2 SCIENTIFIC OBJECTIVES

The LST payload is designed to continuously monitor solar activity and the source regions of space weather drivers, and to image the Sun with high temporo-spatial resolution from the disk center to the inner corona up to 2.5 $R_\odot$ in both the Lyα waveband and WL. The main scientific objectives of the LST payload are to study and answer the following questions.

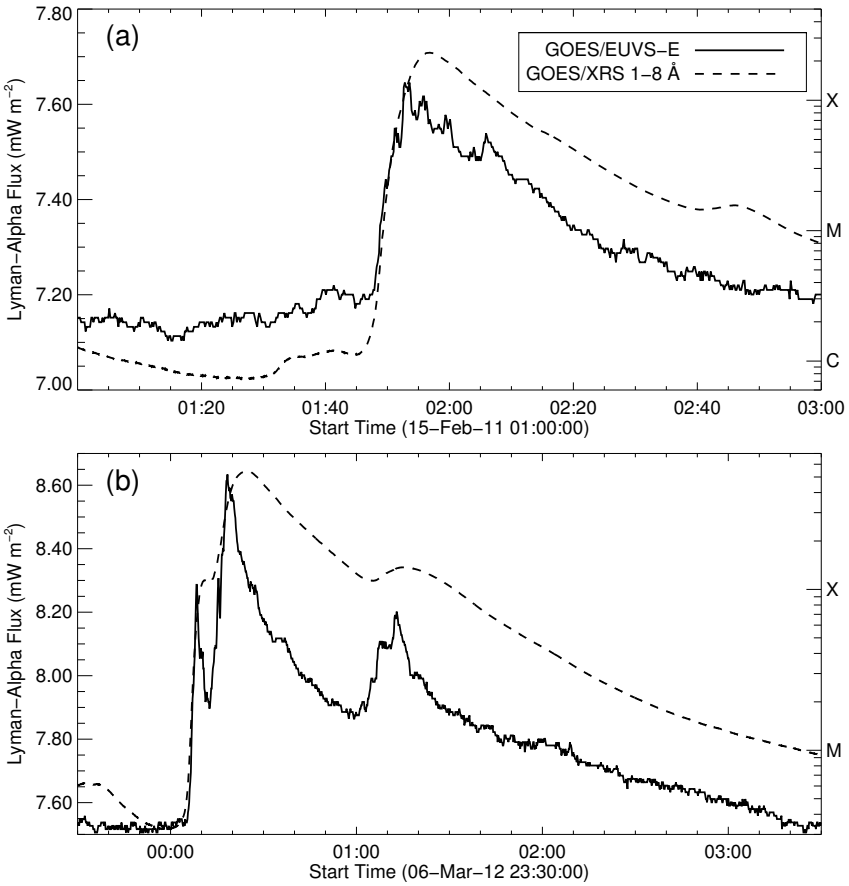

Fig. 1 Lyα irradiance (*solid line*) and 1 – 8 Å X-ray flux (*dashed line*) for (a) the X2.2 flare on 2011 February 15 and (b) the X5.4 and X1.3 flares on 2012 March 7 from GOES observations.

1. What is the relationship between solar flares, CMEs and eruptive prominences?

Solar flares and CMEs, as generally accepted, are powered by free magnetic energy stored in the non-potential current-carrying magnetic field in the solar atmosphere. During flaring processes, particles (electrons, protons, etc.) are accelerated to very high energy (MeV to GeV) and may escape from the solar atmosphere, reach the Earth's upper atmosphere, and subsequently disturb our environment and cause disastrous space weather events.

It is commonly accepted that flares originate locally (at small scale) while CMEs can originate either at small or at large scales. This relationship between solar flares and CMEs has long been under debate but so far it is inconclusive. Some physicists argue that they are just the different manifestations of a single abrupt energy release in the solar atmosphere (e.g., Harrison 1995; Forbes 2000).

Prominence eruption may play a major role in the overall process of solar eruptions, including solar flares and CMEs, via the development of plasma instability and enhancement of magnetic reconnection processes. Is there any causal relationship between flares, CMEs and eruptive prominences? We refer readers to Chapters 12, 15 and 16 of Vial & Engvold (2015) for comprehensive descriptions of triggers for prominence eruption, dynamics of eruptive prominences and the association of eruptive prominences with CMEs. Statistical studies indicate that many flares are not associated with CMEs. For example, it was reported that $\sim$70% of C-class, $\sim$44% of M-class and $\sim$10% of X-class flares are not associated with CMEs (e.g., Wang et al. 2007; Yashiro et al. 2005). Meanwhile, Wang et al. (2011) claimed that about 1/3 of CMEs are not registered by LASCO on SOHO, which increases the difficulty in investigating the relationship. It is also found that the association rate between flares and CMEs increases with the energy of the events (Yashiro & Gopalswamy 2009). LST will image the solar disk and inner corona simultaneously in the same waveband (Lyα) and therefore it is quite suitable for studying the relationship.

2. What triggers solar flares and CMEs, and how do their parameters evolve during the eruptive process?

Even though the energy of flares and CMEs comes from stored free energy, so far, we cannot decisively identify the mechanisms responsible for the release of this

energy. Both solar flares and CMEs are believed to start when the equilibrium of the magnetic configuration in the solar atmosphere is destabilized due to some instability. However, it is a challenge so far to understand the triggering and energy-accumulation mechanisms of these events in the low solar corona, and even in the lower solar atmosphere.

Previous studies have narrowed down the possible CME initiation models to two main classes (see reviews of, e.g., Chen 2011; Webb & Howard 2012), both of which need pre-eruptive current-carrying magnetic field structures. One class assumes that the preexisting structures are sheared arcades (e.g., Antiochos et al. 1999) and for the other class they are flux ropes (e.g., Amari et al. 2014). However, we are still far away from a conclusion. To discriminate between different proposed mechanisms, one needs to observe the CME initiation process in the inner corona and even on the disk.

LST will trace CMEs from their initiation from the disk to the inner corona (up to 2.5 $R_\odot$), observe coronal restructuring during CMEs in detail and measure the CME kinematics. Meanwhile, with observations in both the Lyα line and WL, one will be able to derive the physical parameters of CMEs using proposed and demonstrated algorithms (e.g., Susino & Bemporad 2016; Heinzel et al. 2016; Ying et al. 2019). For more details of the diagnostics with LST data, see Paper III (Feng et al. 2019).

3. What are the acceleration mechanisms of CMEs in the inner corona? What are their kinetic behaviors?

After their initiation, CMEs are accelerated in a short time to high speed (up to more than 2000 km s^{-1}) in the inner corona (Zhang et al. 2001, 2004; Bein et al. 2012) with peak acceleration of more than 600 m s^{-2} (Bein et al. 2011) and may move towards the Earth with vast mass and numerous particles, which may cause severe geomagnetic storms when interacting with the Earth's magnetic field in the upper atmosphere (Schwenn 2006). According to Zhang et al. (2001, 2004), kinetic behaviors of CMEs may display three phases: (a) initiation, (b) major/impulsive acceleration and (c) propagation phases. In phase (a), CMEs initiate with a slow rise, while in phase (b) CMEs are impulsively accelerated to their maximum speed within about 2 $R_\odot$ (e.g., Vršnak 2001). In phase (c), CMEs propagate into interplanetary space with their speed adjusted by the surrounding solar medium (Gopalswamy et al. 2000).

Observations have demonstrated that there is a clear link between the impulsive CME acceleration phase and both the rising phase of soft X-ray flares (Zhang et al. 2001, 2004; Temmer 2016) and particle acceleration (Dauphin et al. 2006; Berkebile-Stoiser et al. 2012). Bearing in mind the relation between CMEs and solar flares, this may indicate that the acceleration of CMEs is possibly related to the released energy during magnetic reconnection of the relevant flares. Therefore, hard X-ray (HXR) observations of CME-related flares could help in understanding the kinetic behavior of CMEs.

Since CMEs initiate in the lower corona and even on the disk when projected onto the plane-of-sky (POS) , we need observations very close to the solar limb and even on the disk to study the early evolution and acceleration of CMEs in detail. LST will provide full-coverage data from the solar disk to the inner corona to address this question. Meanwhile, together with HXR observations from the Hard X-ray Imager (HXI) payload on the ASO-S mission, it will further our understanding about the kinetic behaviors of CMEs.

4. How are shock waves formed and what favors the acceleration of solar energetic particles (SEPs) by shock waves?

When a CME moves faster than the local fast magnetosonic speed, it may drive a shock in front (e.g., Ying et al. 2018). Alternatively, a flare may also drive a blast wave (e.g., Magdalenić et al. 2008). Therefore, the origin of coronal shock waves is still under debate. When a shock forms, it is often associated with a radio type II burst. The dynamic spectra and imaging observations of type II bursts reveal that the shock sometimes forms in the gap between the AIA and LASCO C2 fields-of-view (FOVs) from about 1.2 to 2.2 $R_\odot$ (e.g., Ramesh et al. 2012). Therefore, we are missing imaging observations for these shocks in this critical region. LST will overcome this disadvantage and provide seamlessly valuable observations in both WL and Lyα for studying the origin of shock waves from the solar disk up to 2.5 $R_\odot$.

A shock is an effective accelerator of SEPs. However, we still have not come to a conclusion about what kind of shock properties is favorable for SEP accelerations (e.g., Kozarev et al. 2015). To understand how shock parameters are related to the acceleration of SEPs, the shocks observed by LST are to be used to characterize their standoff distance, shock speed, compression ratio, etc. Together with the global magnetic field extrapolated from the photospheric magnetic field observed from the Full-disk vector MagnetoGraph (FMG) payload, the shock magnetic geometry can be derived to study whether quasi-perpendicular or quasi-parallel shocks are more favorable for SEPs accelerated by a shock. It further helps to understand how, where and when energetic particles get accelerated in shocks traveling through the corona.

5. What are the physical properties and processes of white-light flares (WLFs)?

WLFs are flares with enhancements in the visible continuum, which could contribute a significant fraction of the total radiated energy in the flares (Kretzschmar 2011). It

has been suggested that the continuum brightening may be a common feature for most (if not all) of the flares (e.g., Neidig 1989; Hudson et al. 2006; Jess et al. 2008). WLFs can be classified into two types (Machado et al. 1986; Fang & Ding 1995): Type I exhibits a Balmer (or Paschen) jump in the continuum spectra with an increase towards the blue side and has a good time correlation with the hard X-ray emission (Hudson et al. 2006; Hao et al. 2012; Cheng et al. 2015; Hao et al. 2017), while Type II does not show those features and seems to be less frequently observed (e.g., Ding et al. 1994; Ding 2007). Different emission mechanisms have been proposed to explain the WL continuum for the two types of WLFs. Generally speaking, the continuum emission in Type I WLFs is mostly from hydrogen recombination (i.e., free-bound radiation) in the lower chromosphere, while that for Type II WLFs seems to be produced by negative hydrogen ions in the upper photosphere. In fact, the key question regarding the origin of WLFs is how the lower atmosphere gets heated (Ding 2007). It has been supposed that the lower chromosphere could be heated by electron beam precipitation while the upper photosphere could then be heated through radiative backwarming (e.g., Neidig et al. 1993; Cheng et al. 2010). Besides, Alfvén waves have been proposed as an alternative energy transport mechanism to the lower atmosphere (Fletcher & Hudson 2008). How much the chromospheric condensations contribute to WL emission has also been explored (Gan et al. 1992; Kowalski et al. 2015). In addition, numerical simulations have predicted a negative effect or a darkening in the WL continuum (also called a 'black-light' flare) in the initial phase of the flares (e.g., Henoux et al. 1990; Ding et al. 1994; Ding & Fang 1996; Ding et al. 1999; Hong et al. 2018). However, this has rarely been observed up to now (van Driel-Gesztelyi et al. 1994), probably due to the relatively low temporo-spatial resolution of the current instruments.

LST will provide high-cadence (up to $\sim$1 s) observations in the 360 nm passband, i.e., imaging of the Balmer continuum emission. On the one hand, it can help in studying the origin of WLFs, especially their heating mechanisms, when combined with the HXI/ASO-S observations of nonthermal electrons as well as radiative transfer modeling (a diagnostic tool being developed for LST, see Paper III by Feng et al. 2019). On the other hand, it can help in searching for black-light flares and advancing our understanding of the physical nature of WLFs.

6. What are the physical properties of the CME source region?

Both solar flares and CMEs take place in the very low layer of the solar atmosphere. The physical conditions associated with the source regions of flares and CMEs on the disk determine, to some degree, their behavior and characteristics. LST together with the FMG payload on the ASO-S mission will easily locate the source regions and provide images in both the Lyα line and WL, and vector magnetic field data. These data will allow us to estimate the physical parameters of the source regions based on simulations of the Lyα line formation; and to study the magnetic properties, including shear, helicity, current, free energy, topological configuration, etc.; and further to explore the possible relation between the source region properties and the behavior of eruptions.

3 LST OVERVIEW

Now, we present an overview of the LST payload, including its characteristics and specifications, along with its optical and mechanical layouts. Readers are referred to Paper II (Chen et al. 2019) for details about the LST instrumentation.

3.1 LST Characteristics and Specifications

As mentioned in Section 1, LST consists of three instruments (SDI, SCI and WST) for scientific observations and two GTs for guidance and image stabilization. Such a combination with the specifications below can address the above-mentioned scientific topics well.

Both SDI and WST have an FOV of 1.2 $R_\odot$. SDI has an aperture of 60 mm and works in the Lyα line (121.6$\pm$7.5 nm), while WST has an aperture of 130 mm and operates in the 360$\pm$2 nm waveband. SCI has an aperture of 60 mm, and an FOV of 1.1 – 2.5 $R_\odot$ and operates in both the Lyα line (121.6$\pm$10 nm, SCI_UV hereafter) for imaging and the 700$\pm$40 nm (SCI_WL hereafter) waveband for polarization brightness (pB) measurement. The images taken by SDI and WST have a format of 4608$\times$4608 pixels (only part of the 6144$\times$6144 pixels of the complementary metal oxide semiconductor (CMOS) detectors are read out and stored) while those for both channels of SCI have a format of 2048$\times$2048 pixels. Consequently, the images taken by SDI, WST and SCI will have nominal pixel scales of $\sim$0.5″, $\sim$0.5″ and $\sim$2.4″, respectively. The expected spatial resolutions are $\sim$1.2″, $\sim$1.2″ and $\sim$4.8″, respectively, taking into account the effect of the modulation transfer function for the system and detectors.

We summarize the specifications of LST in Table 1.

3.2 Mechanical Layout

The overall structure of LST is divided into two layers: upper and lower layers (Fig. 2), which share the main board in between. SCI together with its focal plane assembly (FPA), electronics box (EB) and main guide telescope (GT1), is

Table 1 LST Specifications

Parameter	SCI_UV	SCI_WL	SDI	WST	GT
Aperture (mm)	60	60	60	130	30
Wavelength (nm)	121.6±10.0	700±40	121.6±7.5	360.0±2.0	570.0±5.0
FOV ($'$)	35.2 – 80	35.2 – 80	38.4	38.4	38.4
FOV ($R_\odot$)	1.1 – 2.5	1.1 – 2.5	1.2	1.2	1.2
Spatial resolution ($''$)	∼4.8	∼4.8	∼1.2	∼1.2	
Detector sensor	CMOS	CMOS	CMOS	CMOS	photodiodes
Image format	2048×2048	2048×2048	4608×4608	4608×4608	linear array
Cadence (s) (1)	15 – 30	30 – 60(2)	4 – 40	1 – 120	
Estimated exposure (s)(3)	3 – 20	1 – 5	0.1 – 8	0.01 – 0.05	
pB polarizer angle (°)		0, ±60			

(1) Nominal cadence. Other cadences are available on demand with the user mode within instrument limits;
(2) Cadence for a set of pB images, i.e., three images with the angle of the linear polarizer at 0° and ±60°;
(3) Exposure time estimated with current instrument parameters and final exposure times will be determined during the maneuvering phase of the ASO-S mission.

installed on the upper layer while SDI, WST and the spare guide telescope (GT2) are fixed on the lower layer. All the radiators for passive thermal control are on the backside of the LST envelope.

The shared main board is made of silicon carbide composites, which have the characteristics of high strength, high thermal conductivity and low expansion coefficients. Three legs of silicon carbide composites on the main board are used to fix the LST payload to the platform.

3.3 Optical Layouts

SCI is an inner-occulted Lyot-type reflective coronagraph with a clear aperture of 60 mm. Its optical layout is illustrated in Figure 3. The main mirror (M1) images the Sun and inner corona on the secondary mirror (M2), which has a cone-shaped hole in the center working as the inner occulter of the coronagraph. Beams from the solar disk go through the hole and then are trapped and absorbed by the light trap (LT) just behind M2, while those of the inner corona go to the tertiary mirror (M3), which images the corona on the detectors. A specially coated mirror working as a beam splitter (BS), which reflects ultraviolet (UV) light and transmits visible light, subsequently feeds the Lyα and WL channels. Bandpass filters (not shown in Figure 3) are used to select the required wavebands and linear polarizers for pB measurement at polarization angles of 0° and ±60°.

Figure 4 depicts the optical layouts of SDI (in blue, upper part of the figure) and WST (in green, lower part of the figure). They have a clear aperture of 60 mm and 130 mm, respectively. A simple but effective configuration of two mirrors (main mirror M1 and secondary mirror M2) is used to image the Sun on the focal plane. Once again, corresponding bandpass interference filters are employed for wavelength selection. The two GTs have a similar optical layout (not displayed here) but with only a 30 mm clear aperture.

3.4 Image Sensors

All image sensors utilized in the LST payload are of the CMOS type. Due to the very low quantum efficiency (QE) of the CMOS sensor in the Lyα waveband, we coated the sensors with phosphor (Lumogen) for the SCI Lyα channel and SDI, an approach which has been demonstrated to be feasible by the TRACE mission on charge coupled device (CCD) sensors. Our experiment demonstrates that the QE could be doubled after coating. For WST and the WL channel of SCI, CMOS sensors are used without any coating.

The sensors have an analog-to-digital converter (ADC) of 14 bits, which is not sufficient for LST instruments except for WST. WST targets observing WLFs, which just require a narrow dynamical range. Fortunately, the sensors have a high dynamical range (HDR) mode, which allows readout of the image with both low gain (LG) and high gain (HG) simultaneously with a single exposure. With the HDR mode, we can construct images with a dynamical range of 16 bits or larger, depending on the HG/LG ratio. The disadvantage is that the signal-to-noise ratio (SNR) in the constructed image may be discontinuous around the threshold value, i.e., a sensor-related digital value determining whether the HG or LG pixel value should be used in the constructed HDR image.

3.5 Stray-light Suppression of SCI

Stray-light suppression is critical for any coronagraph, including SCI of course. Because the relative intensity (with respect to the mean brightness ($B_\odot$) of the solar disk) of the Lyα line is about 2 – 3 orders of magnitude higher than that of WL, stray-light suppression for WL is much more stringent than that for the Lyα line (see figure 4 of Vial et al. 2007). Simulations indicate that for the SCI WL channel, the stray-light allowed is less than $1.0\times10^{-6}\,B_\odot$ at $1.1\,R_\odot$ and $5.0\times10^{-8}\,B_\odot$ at $2.5\,R_\odot$. To fulfill this requirement, a conjugate design, baffles, a light trap and super-polished

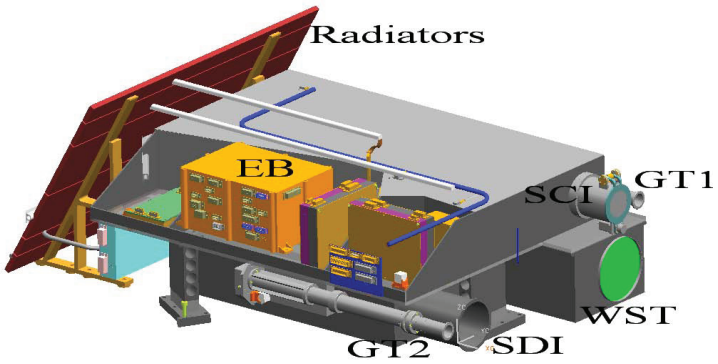

Fig. 2 LST mechanical layout. SDI: Solar Disk Imager; SCI: Solar Corona Imager; WST: White-light Solar Telescope; GT1: Main Guide Telescope; GT2: Spare Guide Telescope; EB: Electronics Box.

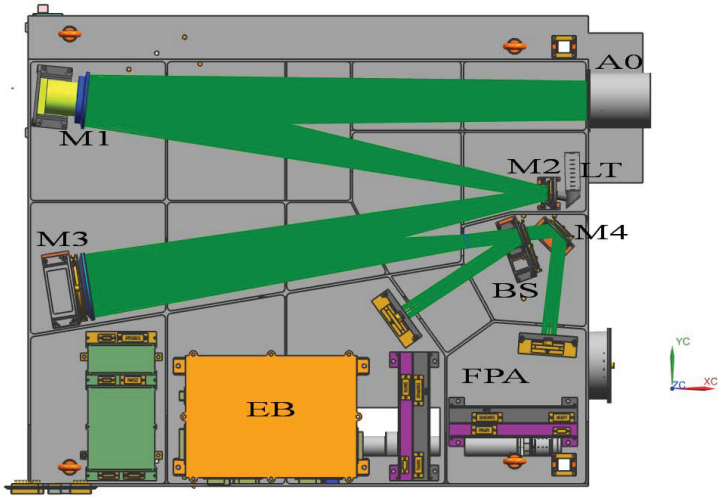

Fig. 3 SCI optical layout. A0: Entrance Aperture; M1: Main Mirror; M2: Secondary Mirror, inner occulter; M3: Tertiary Mirror; M4: Fourth Mirror; LT: Light Trap; BS: Beam Splitter; FPA: Focal Plane Assembly; EB: Electronics Box.

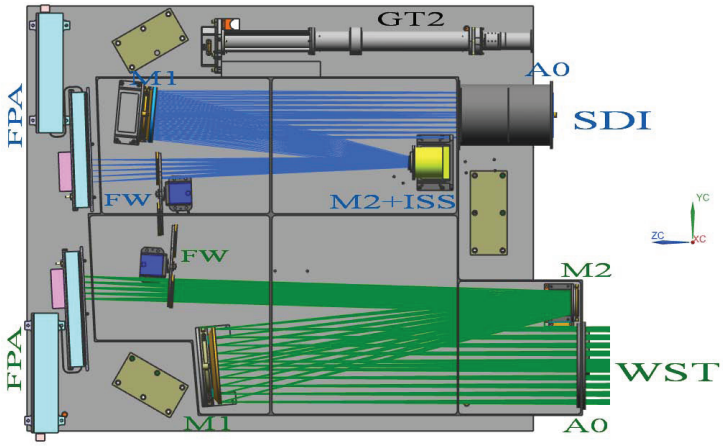

Fig. 4 SDI (*blue*, upper part) and WST (*green*, lower part) optical layout. A0: entrance aperture; M1: main mirror; M2: secondary mirror; ISS: image stabilizing system; FW: filter-wheel; FPA: focal plane assembly.

mirrors (M1 and M2) are employed. Simulations indicate that the current design and mirror parameters fulfill the requirement. We will measure stray-light with the qualification model (QM) to ascertain the requirement is fulfilled. A cleanroom better than class 1000 will be used in the integration processes.

3.6 Image Stabilization

The image stabilizing capability of the platform is not sufficient for the high resolution observations of LST, especially for SDI and SCI, which require high image stability due to the high resolution and/or long exposure. Therefore, both SCI and SDI instruments have their own image stabilizing systems (ISSs), which exploit the signal of the Sun center from the GT and the piezoelectric activator installed behind the main mirror (M1) of SCI and the secondary mirror (M2) of SDI. WST does not have an ISS due to its very short exposure time (on the order of milliseconds) and the image stability requirement can be guaranteed by the platform.

4 LST OBSERVATION MODES

When LST is switched on in orbit, it will be in one of the following working modes: standby, test, eclipse, calibration and observation. The standby and test modes have their common meanings. LST goes into eclipse mode when the satellite enters the shadow of the Earth. The calibration mode will be described in a separate paper. Here, we just describe the observation mode.

LST is fully functional in the observation mode. Generally, LST instruments have three modes for observation: routine mode, event mode and user mode. We introduce these modes one by one in the following subsections.

4.1 Routine Mode

The routine mode is the most commonly used observation mode for all the LST instruments, and is mainly operated to watch the solar disk and inner corona for activity. All the three instruments (SDI, SCI and WST) record full-size images (2048×2048 pixels for SCI and 4608×4608 pixels for SDI and WST) with a moderate cadence of 10 – 30 s (Table 2). Due to the limitation of telemetry, we may download only part of all the images taken in this mode to the ground. Therefore, we set an image download interval (IDI) for the routine mode. The IDI for SDI is 40 s, i.e., we download one of every four images. For WST, one of every twelve images will be downloaded.

The cadence and IDI for SCI in routine mode are average values as explained here. For the SCI_UV channel, we plan to take two images in one minute with different exposure times in order to record both strong and weak features in the corona, which provides an average cadence and IDI of 30 s. For the SCI_WL channel, it will take a set of images in 30 s, i.e., three pB images with the angles of the linear polarizer at $-60°$, $0°$ and $+60°$. One of every two sets will be downloaded, so that we have three images in one minute, which enables an average IDI of 20 s.

4.2 Event Mode

The event mode is designed for observations of the two common kinds of solar eruptions: solar flares and CMEs. LST instruments start event mode observation when a trigger signal is received from the onboard computer of the ASO-S mission.

Solar flares and CMEs generally do not happen concurrently, so they need different trigger signals for the event mode. SDI and WST change to event mode according to a trigger signal of flares, which comes from SDI and HXI also onboard ASO-S. SDI monitors the full disk and detects flare initiation based on the brightness change of images obtained in the Lyα waveband. It provides trigger signals and the location of the flare as well, with the proposed algorithm to be presented and discussed in a separate paper later. Once they receive a trigger signal, SDI and WST conduct windowed observation, which is referred to as event-W mode. In more detail, the detectors of SDI and WST read out and save only a portion of the image, which is 1024×1024 pixels by default (Table 2). HXI can only provide a trigger signal of a flare without location information. Therefore, the trigger signal from HXI has less priority. Consequently, if the trigger signal comes from HXI, SDI and WST cannot conduct a windowed observation but do record and save the full-size images. We refer to this as event-F mode.

SCI enters the event mode according to trigger signals from SCI_WL observation. SCI_WL monitors the inner corona and executes a proposed algorithm to detect the onset of CMEs based on the brightness change of obtained images in the WL waveband. In event mode, SCI records and saves full-size images with a higher cadence (c.f. Table 2).

When solar flares and CMEs happen, the brightness of the flaring area and CMEs in the Lyα waveband may increase significantly. Therefore, in event mode, the SDI and SCI_UV channels exploit an automatic exposure control (AEC) algorithm to control the exposure time so as to keep saturated pixels in the obtained images at a minimum level. Description of the AEC algorithm is beyond the scope of this paper.

Table 2 LST Observation Mode Summary

Instrument	Mode	Cadence (s)	Image download interval (s)	Image size (pixels)	A/D (bit)
SDI	Routine	10	40	4608×4608	14
	Event-W	4	4	1024×1024	14
	Event-F	10	10	4608×4608	14
	User	user-defined	user-defined	512×512 – 4096×4096	14
SCI_UV	Routine	30 (average)	30 (average)	2048×2048	14
	Event	15	15	4608×4608	14
	User	user-defined	user-defined	512×512 – 2048×2048	14
SCI_WL	Routine	10 (average)	20 (average)	2048×2048	14
	Event	10	10	2048×2048	14
	User	user-defined	user-defined	512×512 – 2048×2048	14
WST	Routine	10	120	4608×4608	14
	Event-W	1 or 2	1 or 2	1024×1024	14
	Event-F	5	5	4608×4608	14
	User	user-defined	user-defined	512×512 – 4096×4096	14

Notes: Please refer to the text for an explanation of event-W and event-F modes and other parameters in the table.

4.3 User Mode

With the LST observation data, many scientific topics will be addressed. Various scientific questions, of course, define diverse observation requirements, including changing cadence, exposure time, image size, instrument combination, etc. The user mode of LST observation is proposed to fulfill these requirements and to widen the scientific research scope of LST data. The cadence, IDI and image size can be defined by users within the capability of the instruments. Note that the minimum allowed image size is 512×512 pixels, and the allowed pixel number in both the horizontal and vertical directions must be 2^n (n = 9, 10 and 11 for SCI and 9, 10, 11 and 12 for SDI and WST). Nevertheless, the pixels in the two directions can be different. The possible cadences and IDIs will be detailed in the future.

5 SUMMARY

In this paper, we present the scientific objectives, instrument overview and observation modes of the LST payload for the ASO-S mission. As one of the three payloads of the mission, LST will open a new window with the Lyα line to image the full-disk Sun and the inner corona up to 2.5 $R_\odot$ without gaps continuously and simultaneously with high temporo-spatial resolution.

Together with observations in other wavebands (360 nm and 700 nm), it is foreseen that LST will contribute to the study of the initiation, evolution and kinetics of solar flares and CMEs, of the relation between flares, prominence eruptions and CMEs, and of the interface region between the corona and the chromosphere among other objectives. With observations in both the Lyα line (imaging) and WL (pB), LST will be able to obtain the electron density and temperature distribution of the inner corona in various structures.

Acknowledgements The ASO-S mission was formally approved by the Chinese Academy of Sciences (CAS) in December of 2017 and is scheduled to be launched in early 2022. All payloads of the ASO-S mission are now in phase C study. The LST payload derives heritage from the Lyman-alpha Orbital Telescope (LYOT) for the once proposed French-Chinese SMall Explorer for Solar Eruptions (SMESE) (Vial et al. 2007) mission. This work is supported by the National Natural Science Foundation of China (Grant Nos. 11427803 and U1731241) and by the CAS Strategic Pioneer Program on Space Science (Grant Nos. XDA04061003, XDA04076100, XDA15052200, XDA15320103 and XDA15320301).

References

Amari, T., Canou, A., & Aly, J.-J. 2014, Nature, 514, 465
Antiochos, S. K., DeVore, C. R., & Klimchuk, J. A. 1999, ApJ, 510, 485
Antonucci, E., Romoli, M., Andretta, V., et al. 2019, A&A, in press
Bein, B. M., Berkebile-Stoiser, S., Veronig, A. M., et al. 2011, ApJ, 738, 191
Bein, B. M., Berkebile-Stoiser, S., Veronig, A. M., Temmer, M., & Vršnak, B. 2012, ApJ, 755, 44
Berkebile-Stoiser, S., Veronig, A. M., Bein, B. M., & Temmer, M. 2012, ApJ, 753, 88
Brueckner, G. E., Howard, R. A., Koomen, M. J., et al. 1995, Sol. Phys., 162, 357
Chen, B., Li, H., Song, K., et al. 2019, RAA (Research in Astronomy and Astrophysics), 19, 159
Chen, P. F. 2011, Living Reviews in Solar Physics, 8, 1
Cheng, J. X., Ding, M. D., & Carlsson, M. 2010, ApJ, 711, 185
Cheng, X., Hao, Q., Ding, M. D., et al. 2015, ApJ, 809, 46
Dauphin, C., Vilmer, N., & Krucker, S. 2006, A&A, 455, 339
Delaboudinière, J.-P., Artzner, G. E., Brunaud, J., et al. 1995, Sol. Phys., 162, 291

Ding, M. D. 2007, in Astronomical Society of the Pacific Conference Series, 368, The Physics of Chromospheric Plasmas, eds. P. Heinzel, I. Dorotovič, & R. J. Rutten, Heinzel
Ding, M. D., & Fang, C. 1996, A&A, 314, 643
Ding, M. D., Fang, C., Gan, W. Q., & Okamoto, T. 1994, ApJ, 429, 890
Ding, M. D., Fang, C., & Yun, H. S. 1999, ApJ, 512, 454
Dolei, S., Susino, R., Sasso, C., et al. 2018, A&A, 612, A84
Domingo, V., Fleck, B., & Poland, A. I. 1995, Sol. Phys., 162, 1
Esser, R., & Habbal, S. R. 1993, Sol. Phys., 147, 241
Fang, C., & Ding, M. D. 1995, A&AS, 110, 99
Feng, L., Li, H., Chen, B., et al. 2019, RAA (Research in Astronomy and Astrophysics), 19, 162
Fletcher, L., & Hudson, H. S. 2008, ApJ, 675, 1645
Forbes, T. G. 2000, J. Geophys. Res., 105, 23153
Gan, W. Q., Rieger, E., Zhang, H. Q., & Fang, C. 1992, ApJ, 397, 694
Gan, W., Zhu, C., Deng, Y. Y., et al. 2019, RAA (Research in Astronomy and Astrophysics), 19, 156
Gopalswamy, N., Lara, A., Lepping, R. P., et al. 2000, Geophys. Res. Lett., 27, 145
Handy, B. N., Tarbell, T. D., Wolfson, C. J., Korendyke, C. M., & Vourlidas, A. 1999a, Sol. Phys., 190, 351
Handy, B. N., Acton, L. W., Kankelborg, C. C., et al. 1999b, Sol. Phys., 187, 229
Hao, Q., Guo, Y., Dai, Y., et al. 2012, A&A, 544, L17
Hao, Q., Yang, K., Cheng, X., et al. 2017, Nature Communications, 8, 2202
Harrison, R. A. 1995, A&A, 304, 585
Heinzel, P., Susino, R., Jejčič, S., Bemporad, A., & Anzer, U. 2016, A&A, 589, A128
Henoux, J.-C., Aboudarham, J., Brown, J. C., van den Oord, G. H. J., & van Driel-Gesztelyi, L. 1990, A&A, 233, 577
Hong, J., Ding, M. D., Li, Y., & Carlsson, M. 2018, ApJ, 857, L2
Hong, J., Li, Y., Ding, M. D., & Carlsson, M. 2019, arXiv:1905.13356
Howard, R. A., Moses, J. D., Vourlidas, A., et al. 2008, Space Sci. Rev., 136, 67
Hudson, H. S., Wolfson, C. J., & Metcalf, T. R. 2006, Sol. Phys., 234, 79
Hyder, C. L., & Lites, B. W. 1970, Sol. Phys., 14, 147
Jess, D. B., Mathioudakis, M., Crockett, P. J., & Keenan, F. P. 2008, ApJ, 688, L119
Kaiser, M. L., Kucera, T. A., Davila, J. M., et al. 2008, Space Sci. Rev., 136, 5
Kowalski, A. F., Hawley, S. L., Carlsson, M., et al. 2015, Sol. Phys., 290, 3487
Kozarev, K. A., Raymond, J. C., Lobzin, V. V., & Hammer, M. 2015, ApJ, 799, 167
Kretzschmar, M. 2011, A&A, 530, A84
Lemen, J. R., Title, A. M., Akin, D. J., et al. 2012, Sol. Phys., 275, 17
Li, H. 2016, in IAU Symposium, 320, Solar and Stellar Flares and their Effects on Planets, ed. A. G. Kosovichev, S. L. Hawley, & P. Heinzel, 436
Machado, M. E., Avrett, E. H., Falciani, R., et al. 1986, in The Lower Atmosphere of Solar Flares, eds. D. F. Neidig, & M. E. Machado, 483
Magdalenić, J., Vršnak, B., Pohjolainen, S., et al. 2008, Sol. Phys., 253, 305
Neidig, D. F. 1989, Sol. Phys., 121, 261
Neidig, D. F., Kiplinger, A. L., Cohl, H. S., & Wiborg, P. H. 1993, ApJ, 406, 306
Pesnell, W. D., Thompson, B. J., & Chamberlin, P. C. 2012, Sol. Phys., 275, 3
Ramesh, R., Lakshmi, M. A., Kathiravan, C., Gopalswamy, N., & Umapathy, S. 2012, ApJ, 752, 107
Schühle, U., Halain, J.-P., Meining, S., & Teriaca, L. 2011, in Society of Photo-Optical Instrumentation Engineers (SPIE) Conference Series, 8148, Solar Physics and Space Weather Instrumentation IV, 81480K
Schwenn, R. 2006, Living Reviews in Solar Physics, 3, 2
Susino, R., & Bemporad, A. 2016, ApJ, 830, 58
Temmer, M. 2016, Astronomische Nachrichten, 337, 1010
van Driel-Gesztelyi, L., Hudson, H. S., Anwar, B., & Hiei, E. 1994, Sol. Phys., 152, 145
Vial, J.-C., & Engvold, O., eds. 2015, Astrophysics and Space Science Library, 415, Solar Prominences
Vial, J.-C., Auchère, F., Chang, J., et al. 2007, Advances in Space Research, 40, 1787
Vourlidas, A., Sanchez Andrade-Nuño, B., Landi, E., et al. 2010, Sol. Phys., 261, 53
Vourlidas, A., Beltran, S. T., Chintzoglou, G., et al. 2016, Journal of Astronomical Instrumentation, 5, 1640003
Vršnak, B. 2001, Sol. Phys., 202, 173
Wang, H., Liu, C., Jing, J., & Yurchyshyn, V. 2007, in American Astronomical Society Meeting Abstracts, 210, 93.21
Wang, Y., Chen, C., Gui, B., et al. 2011, Journal of Geophysical Research (Space Physics), 116, A04104
Webb, D. F., & Howard, T. A. 2012, Living Reviews in Solar Physics, 9, 3
Woods, T. N., Eparvier, F. G., Hock, R., et al. 2012, Sol. Phys., 275, 115
Yashiro, S., & Gopalswamy, N. 2009, in IAU Symposium, 257, Universal Heliophysical Processes, eds. N. Gopalswamy, & D. F. Webb, 233
Yashiro, S., Gopalswamy, N., Akiyama, S., et al. 2005, Journal of Geophysical Research (Space Physics), 110, A12S05
Ying, B., Bemporad, A., Giordano, S., et al. 2019, arXiv:1905.11772
Ying, B., Feng, L., Lu, L., et al. 2018, ApJ, 856, 24
Zhang, J., Dere, K. P., Howard, R. A., Kundu, M. R., & White, S. M. 2001, ApJ, 559, 452
Zhang, J., Dere, K. P., Howard, R. A., & Vourlidas, A. 2004, ApJ, 604, 420